J. Fluid Mech. (2014), *vol.* 750, *pp.* 99–112.
doi:10.1017/jfm.2014.234

The high-Reynolds-number asymptotic development of nonlinear equilibrium states in plane Couette flow

Kengo Deguchi and Philip Hall†

Department of Mathematics, Imperial College London, South Kensington Campus, London SW7 2AZ, UK

(Received 20 November 2013; revised 3 March 2014; accepted 22 April 2014; first published online 30 May 2014)

The relationship between nonlinear equilibrium solutions of the full Navier–Stokes equations and the high-Reynolds-number asymptotic vortex–wave interaction (VWI) theory developed for general shear flows by Hall & Smith (*J. Fluid Mech.*, vol. 227, 1991, pp. 641–666) is investigated. Using plane Couette flow as a prototype shear flow, we show that all solutions having $O(1)$ wavenumbers converge to VWI states with increasing Reynolds number. The converged results here uncover an upper branch of VWI solutions missing from the calculations of Hall & Sherwin (*J. Fluid Mech.*, vol. 661, 2010, pp. 178–205). For small values of the streamwise wavenumber, the converged lower-branch solutions take on the long-wavelength state of Deguchi, Hall & Walton (*J. Fluid Mech.*, vol. 721, 2013, pp. 58–85) while the upper-branch solutions are found to be quite distinct, with new states associated with instabilities of jet-like structures playing the dominant role. Between these long-wavelength states, a complex 'snaking' behaviour of solution branches is observed. The snaking behaviour leads to complex 'entangled' states involving the long-wavelength states and the VWI states. The entangled states exhibit different-scale fluid motions typical of those found in shear flows.

Key words: general fluid mechanics, mathematical foundations, nonlinear instability

1. Introduction

This paper concerns the manner in which nonlinear equilibrium solutions associated with shear flows at finite Reynolds number deform in the high-Reynolds-number limit. Such solutions have been investigated in plane Couette flow by a number of authors, dating back to Nagata (1990) and more recently including Waleffe (2003), Wang, Gibson & Waleffe (2007), Gibson, Halcrow & Cvitanovic (2009) and Schneider, Gibson & Burke (2010), for example. These solutions are sometimes referred to as 'exact coherent structures' and were classified as lower- or upper-branch solutions by following them back to the saddle–node bifurcation describing their birth. The lower-branch solutions were subsequently found to play the role of edge states separating laminar and turbulent attractors (see Itano & Toh 2001; Skufca, Yorke & Eckhardt 2006), whilst upper-branch solutions produce bifurcation cascades of new

† Email address for correspondence: philhall@ic.ac.uk

solutions which eventually lead to the formation of chaotic sets (Kreilos & Eckhardt 2012).

At about the same time as Nagata (1990) produced the first equilibrium states for plane Couette flow, Hall & Smith (1989, 1990, 1991) independently laid down a formal asymptotic fully nonlinear framework for what was described as vortex–wave interaction theory (VWI). The framework given is a quite general approach and can be applied to both inviscid (Rayleigh) and viscous (Tollmien–Schlichting) waves interacting with streamwise vortices. Motivated by the numerical results of Wang *et al.* (2007), Hall & Sherwin (2010, hereafter referred to as HS) applied the Hall & Smith (1991) formulation to plane Couette flow and showed that the high-Reynolds-number fates of the lower-branch nonlinear equilibrium solutions were simply vortex–Rayleigh wave interaction states which could be predicted with remarkable accuracy by numerical solution of the VWI equations. The work of HS was subsequently extended to a range of spanwise wavenumbers by Blackburn, Hall & Sherwin (2013), and it was shown that as the spanwise wavenumber β increases, the VWI states deform into canonical states localized away from any boundaries and satisfying the Kolmogorov 5/3 law. However, as was the case in HS, only a single lower-branch state was found for a given streamwise wavenumber α in a range $(0, \alpha_c(\beta))$, and the question of whether there is an upper-branch asymptotic state beyond the turning point $\alpha = \alpha_c$ was left unanswered.

At long streamwise wavelengths of size comparable to the Reynolds number, the VWI theory fails and the states become long-wavelength asymptotic structures as described by Deguchi, Hall & Walton (2013). Henceforth, we refer to that paper as DHW, where it was found that as α decreased the solutions could not be continued indefinitely, because spatial localization in the streamwise direction occurred, with the flow having the tendency to develop an $O(1)$ streamwise length scale excluded from the long-wavelength theory.

Here we resolve all the issues surrounding the fate of equilibrium solutions of plane Couette flow in the high-Reynolds-number limit. In the next section we will write down the equations of motion and the briefest of descriptions of our numerical procedure. The VWI theory and the long-wavelength theory are formally valid as the Reynolds number goes to infinity, and the challenge is to see how the finite-but-large-R calculations conform with those asymptotic predictions. Section 3 concerns the development of the equilibrium solutions towards the VWI asymptotic structure, and in § 4 we show how the VWI structure fails at small α. Finally, in § 5, we draw some conclusions.

2. Formulation of the problem

We are concerned with solutions of the Navier–Stokes equations in a channel with rigid walls moving in opposite directions at equal speeds. Couette flow is a solution to this problem, but here we seek more general steady solutions periodic in the x and z directions with respect to Cartesian coordinates with wavenumbers α and β, respectively. We take the steady Navier–Stokes and continuity equations written in the form

$$(\boldsymbol{u}\cdot\boldsymbol{\nabla})\boldsymbol{u} = -\boldsymbol{\nabla}p + R^{-1}\nabla^2\boldsymbol{u}, \quad \boldsymbol{\nabla}\cdot\boldsymbol{u} = 0. \tag{2.1a,b}$$

Here R is the Reynolds number (based on the half-height of the channel and the wall speed) and we have taken Cartesian coordinates x, y, z with the x axis pointing in the direction of motion of the walls and y and z measuring dimensionless distance in the

normal and spanwise directions, respectively. The velocity field $\boldsymbol{u}$ satisfies the no-slip conditions

$$\boldsymbol{u} = (\pm 1, 0, 0) \quad \text{at } y = \pm 1. \tag{2.2}$$

The numerical approach used here has been developed over a number of years by Nagata and his colleagues. In the present case, the implementation of the code is close to that described in DHW. The method utilizes a Galerkin spectral approach with Chebyshev polynomials used in the normal direction and Fourier series in the other two directions. Newton iteration was used to find equilibrium solutions with the initial guess provided by a 'nearby' already-computed solution, beginning with the well-known solutions due to Nagata (1990). The iteration is terminated when the norm of the residual normalized by the norm of the linear part of the equations becomes smaller than 10^{-10}. The number of modes used in each direction to achieve graphical accuracy was of course constantly monitored, and the level of approximation needed for different configurations will be given. Our computations typically ensure three-digit accuracy for the wall drag correction. In order to follow the solution branches at small streamwise wavenumbers, $\alpha \lesssim 0.2$, 90 streamwise modes were needed. On the other hand, for moderate wavenumbers at high Reynolds number where the solutions have a sharp structure in the y–z plane, the maximum number of basis functions used in the y and z directions were 120 and 40, respectively.

3. The approach to VWI states at increasing Reynolds numbers

The high-R theory of Hall & Smith (1991) shows that the stationary VWI solution of (2.1) takes the form

$$\boldsymbol{u} = [U, R^{-1}V, R^{-1}W](y, z) + R^{-7/6}\widetilde{\boldsymbol{u}}(x, y, z) + \cdots, \tag{3.1a}$$

$$p = R^{-2}P(y, z) + R^{-7/6}\widetilde{p}(x, y, z) + \cdots, \tag{3.1b}$$

where U is the streak flow, $[V, W]$ is a two-dimensional roll flow, $\widetilde{\boldsymbol{u}}$ is a three-dimensional wave and P and $\widetilde{p}$ are the corresponding pressure fields. The roll, streak and wave are taken to be periodic in $x \in [0, 2\pi/\alpha]$ and $z \in [0, 2\pi/\beta]$. The key feature of VWI is the decoupling of the vortex system

$$(V\partial_y + W\partial_z)U = (\partial_{yy}^2 + \partial_{zz}^2)U, \tag{3.2}$$

$$(V\partial_y + W\partial_z)V = -\partial_y P + (\partial_{yy}^2 + \partial_{zz}^2)V, \tag{3.3}$$

$$(V\partial_y + W\partial_z)W = -\partial_z P + (\partial_{yy}^2 + \partial_{zz}^2)W, \tag{3.4}$$

$$\partial_y V + \partial_z W = 0 \tag{3.5}$$

and the wave system, which can be reduced to the pressure form of Rayleigh's equation,

$$\boldsymbol{\nabla} \cdot \left(\frac{\boldsymbol{\nabla}\widetilde{p}}{U^2} \right) = 0, \tag{3.6}$$

with vanishing normal derivative of $\widetilde{p}$ at the boundaries.

The equation for the wave becomes singular at $y = f(z)$ where $U(f(z), z) = 0$ and is smoothed out by a thin viscous critical layer of thickness $O(R^{-1/3})$. Within the critical layer, the wave's Reynolds stresses drive the roll flow so that (3.3)–(3.5) must be solved subject to stress jumps across the critical layer. The amplitude of the wave, $O(R^{-7/6})$, is fixed by the condition that the jump in the roll stress across the critical

layer is comparable with the roll stress elsewhere in the flow. The reader is referred to HS for the stress jumps; here we simply note that they are functions of the wave pressure $\widetilde{p}$ evaluated on the critical layer. Another important feature of (3.6) is that the wave satisfies a linear equation and so only one streamwise Fourier mode plays a role in the VWI.

This three-pointed interaction occurs in a wide range of internal or external flows, and therefore we believe the results in this paper are generally applicable to any shear flow. The same coupling was later identified by Waleffe (1997) through analysing numerical results of equilibrium solutions at finite Reynolds number and became accepted as the underlying physical mechanism underpinning what came to be known as the 'self-sustained process'. HS showed that the mechanism described by Waleffe, where the production of the wave is explained by the linear instability of the streak rather than (3.6), was a finite-Reynolds-number interpretation of the high-Reynolds-number VWI approach.

The equilibrium solution we investigate corresponds to $\beta = 2$ and is the lower-branch solution investigated by Wang *et al.* (2007) and HS. The wall drag Δ, averaged in the x and z directions and normalized by its laminar value, is chosen as a measure of the solutions. We follow solutions in the α–Δ plane at Reynolds numbers beyond the critical one where they begin as a saddle–node bifurcation. The solutions initially form a closed oval shape; see, for example, the curve for $R = 200$ shown in figure 1(*a*). The results shown in the same plot for $R = 400$ and 500 confirm that the lower branches are quickly converging to the state found by HS. At $R = 500$ we observe the beginning of a complex 'snaking' behaviour of the solution branch at smaller values of α. Note that though the curve appears quite sharp at some points, it is in fact smooth and therefore represents the same solution family. We first discuss the asymptotic convergence of the solution with respect to R away from the long-wavelength states whose complicated structure will be discussed in the next section.

The nature of the behaviour at higher Reynolds numbers is shown in figure 1(*b*) for $R = 1000$, 10 000 and 16 000. The continuation of the solution branch further into the snaking region existing at small α was abandoned because the requirement of high resolution proved too computationally expensive; the typical truncation level in the x, y and z directions used to compute the snaking branch for $R = 500$ was 90, 40 and 16, respectively. It is clear that the lower-branch results have converged to the HS state. Surprisingly, we see in figure 1(*c*) that by increasing R up to 40 000, the computations also converge to an upper branch not found by HS (note that the results in the figure are the more accurate solutions of the HS problem found by Isoni 2014). This upper limiting curve connects with the lower-branch HS solutions. The results of figure 1(*a*,*b*) also show that at small α there is no convergence to the VWI state and that the complicated solution branches which develop there begin at smaller α as R increases. Notice here that figure 1(*c*) shows an accurate prediction of the limiting curve for α of $O(1)$ and R up to 40 000; higher values of R are needed to further extend the VWI curve at smaller wavenumbers.

In order to confirm the convergence toward the VWI states, we define E_n as the average energy of the nth streamwise Fourier mode in a periodic box. Then, for VWI states, $E_1 \gg E_n$ for $n = 2, 3, \ldots$ because only the fundamental streamwise Fourier mode is involved at leading order. The energy ratio E_2/E_1 is $O(R^{-1})$ in VWI theory, a result which follows by noticing that at higher order we find that the amplitude of the second-harmonic wave in the critical layer scales as $R^{-4/3}$. Figure 2 shows E_2/E_1 for the results of figure 1(*a*,*b*). We see that as the Reynolds number increases, E_2/E_1 becomes small except for small values of α; this is consistent with the solutions being VWI states.

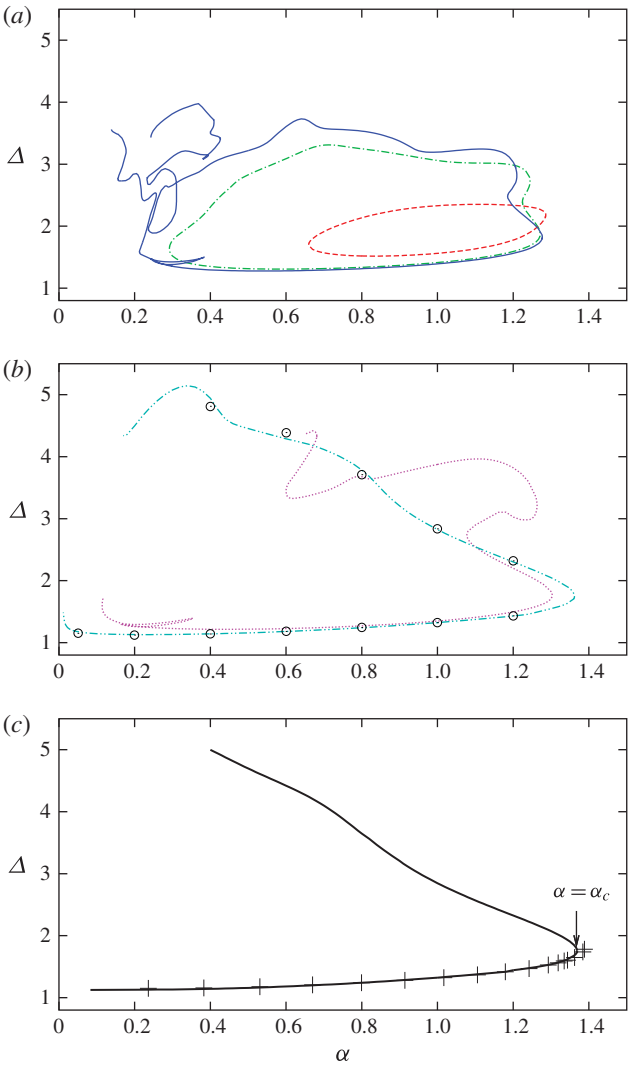

FIGURE 1. Bifurcation diagram of solutions against the wavenumber α using the wall drag Δ as a measure. (*a*) The red dashed, green dot–dashed and blue solid curves are for $R = 200$, 400 and 500, respectively. (*b*) The dotted magenta curve, double-dot–dashed cyan curve and open circles are for $R = 1000$, 10 000 and 16 000, respectively. (*c*) The asymptotically converged result confirmed for R up to 40 000 (solid line) and the corresponding HS values (crosses) as recently computed by Isoni (2014); the turning point is indicated by an arrow.

It is instructive to look at the flow regimes in order to understand more about the changes in the nature of the interaction along the curves of figure 1(*a*,*b*). Figure 3 shows the streak, roll and wave for selected points along the upper and lower branches for $R = 16\,000$. In each panel, the upper plot shows the streak velocity (contours) and roll velocity (arrows) while the lower plot shows contours of the magnitude of the wave Reynolds stress $F = (F_y^2 + F_z^2)^{1/2}$, where F_y and F_z are the Reynolds stresses acting on the y and z components of the roll, respectively. For finite R, the Reynolds

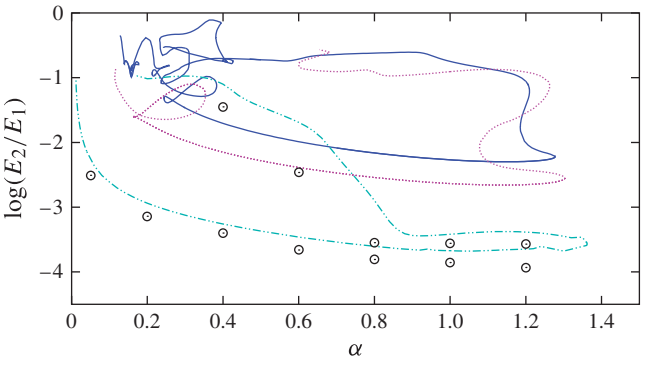

FIGURE 2. Variation of the ratio between the first- and second-harmonic energy functions, E_2/E_1, along the solution branch. The definition of the curves is the same as in figure 1, i.e. the blue solid curve, dotted magenta curve, double-dot–dashed cyan curve and open circles are for $R = 500$, 1000, 10 000 and 16 000, respectively.

stresses F_y and F_z can be computed as the residuals of the roll equations (3.3) and (3.4), respectively. In the VWI theory, F becomes localized in the critical layer and drives the stress jumps in the roll components.

Figure 3(*d–f*) show the corresponding results on the lower branch. We first note that the equilibrium solutions along the lower branch are consistent with VWI theory in that the waves are concentrated in the thin critical layer around $y = f(z)$ (white curves in the lower plots of the panels), where their Reynolds stresses drive the rolls. Note that in the plot for the longest-wavelength $\alpha = 0.05$, the critical layer is now thickening as the DHW regime is approached; see the next section for more discussion of this point.

After the turning point where $\alpha = \alpha_c \approx 1.37$, the solutions develop along an upper branch as shown in figure 3(*a–c*). In the visualization at the point closest to the turning point, i.e. at $\alpha = 1.2$, we see that the solution is clearly of VWI type but with the critical layer now becoming inflected. When $\alpha = 0.8$, we observe that the wave is no longer concentrated in just the critical layer. The concentration of the wave in the critical layer continues in the upper part of the critical layer, but now there is a region away from the inflected parts of the layer where the wave has localized vertically. At the lowest value of $\alpha = 0.4$, this process has continued, with the wave no longer being concentrated anywhere along the critical layer; however, there is an intense region again concentrated away from the critical layer. To check the fate of the upper-branch solutions at high R, we have examined how the flow structure for $\alpha = 0.8$ changes as the Reynolds number increases; the results are shown in figure 4. Since the forcing away from the critical layer diminishes, we see that for fixed α the flow returns to being a VWI state as the Reynolds number increases.

The convergence to the VWI state is also confirmed in figure 5(*a*,*b*) for $\alpha = 0.8$ where typical measures of the roll, streak and wave amplitudes were given. Moreover, the figure suggests that there is also a snaking region on the upper branch. We abandoned the computation of the snaking branch because of resolution issues. The results indicate that after the snaking region, the VWI scaling is retrieved for both upper and lower branches. We therefore interpret the results in figure 3 at the highest value of $\alpha = 1.2$ as a VWI state and the result at the next-highest value of $\alpha = 0.8$ as a VWI state contaminated by some high-R asymptotic state associated with a kind

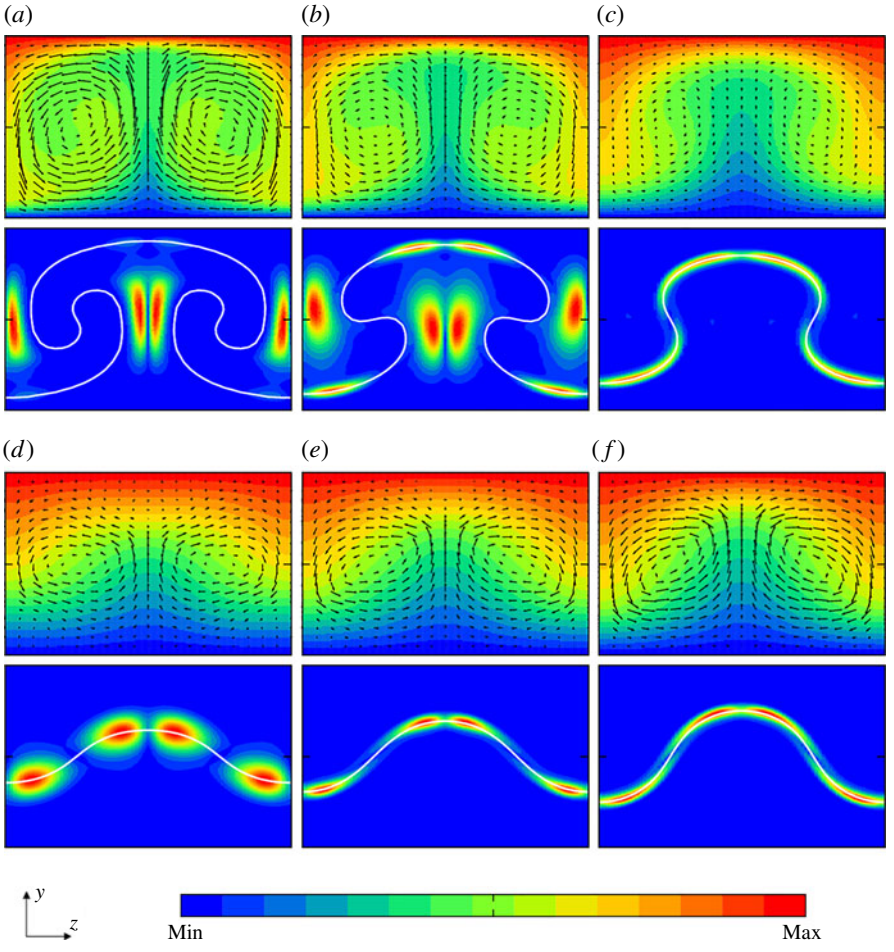

FIGURE 3. The vortex field and wave forcing of the solutions in the y–z plane for $R = 16\,000$: (*a,b,c*) upper branch for $\alpha = 0.4, 0.8$ and 1.2, respectively; (*d,e,f*) lower branch for $\alpha = 0.05, 0.8$ and 1.2, respectively. In each panel, the upper plot depicts U (colour scale) and $[V, W]$ (arrows), while the lower plot shows the wave forcing F, with the critical-layer position indicated by a white curve. Note that the unit length of arrows is different for the upper and lower branches.

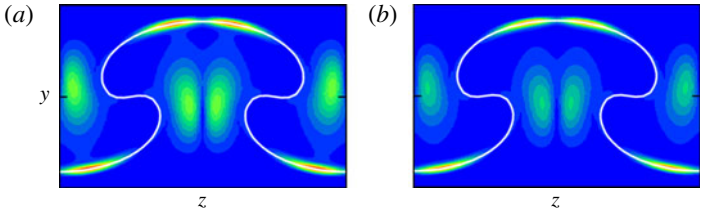

FIGURE 4. Convergence of the upper-branch solution to the VWI structure for $\alpha = 0.8$. The wave forcing F is pictured for (*a*) $R = 30\,000$ and (*b*) $R = 40\,000$.

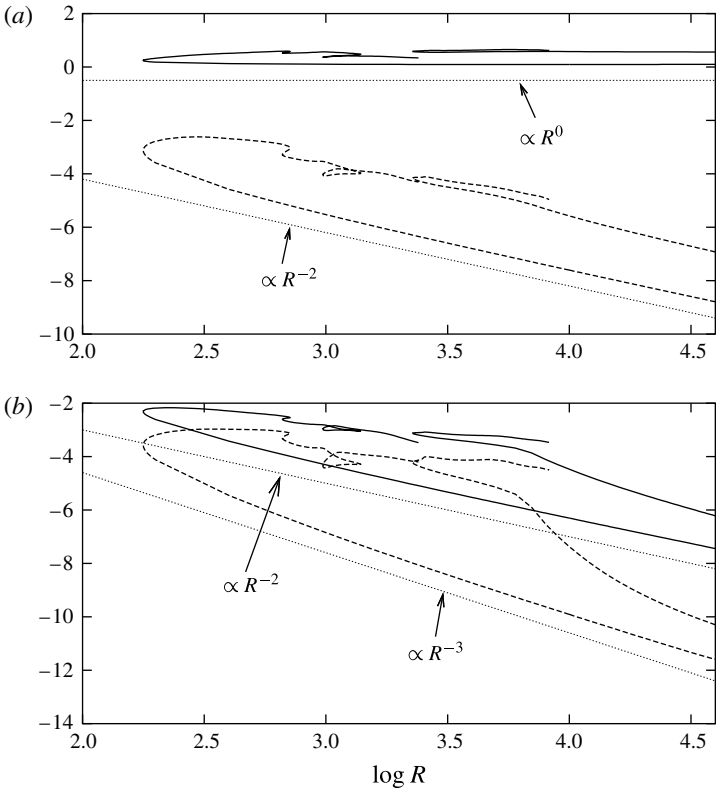

FIGURE 5. High-Reynolds-number scalings of the numerical solutions for $\alpha = 0.8$. (*a*) The solid curve corresponds to $\log(\Delta)$ and is determined by the scaling of the streak; the dashed curve represents $\log(E_{roll})$, where E_{roll} is the energy density associated with the roll components. (*b*) The solid and dashed curves are the energy densities associated with the first and second wave components, $\log(E_1)$ and $\log(E_2)$, respectively; the VWI scaling $\Delta \sim O(1)$, $E_{roll} \sim O(R^{-2})$, $E_1 \sim O(R^{-2})$ and $E_2 \sim O(R^{-3})$ is indicated by the thin dotted lines.

of long-wavelength structure. The nature of that long-wavelength structure, as seen in the plot for $\alpha = 0.4$, will be also discussed in the next section. However, we believe that at this value of α, calculations at higher R would show the solution becoming a VWI state. With our present computational power, resolution issues prevent us from confirming that belief. The truncation levels in the x, y and z directions used for the upper-branch solutions for $\alpha = 0.8$ and $R = 40\,000$ were 7, 120 and 50, respectively.

4. The long-wavelength breakdown of the VWI states

At a small streamwise wavenumber of $O(R^{-1})$, VWI formally fails and the flow associated with the lower-branch solutions of HS is then given by the DHW long-wavelength asymptotic state

$$\boldsymbol{u} = [\widehat{u}, R^{-1}\widehat{v}, R^{-1}\widehat{w}](X, y, z) + \cdots, \quad p = R^{-2}\widehat{p}(X, y, z) + \cdots, \tag{4.1a,b}$$

with $X = R^{-1}x \in [0, 2\pi/(\alpha R)]$ and the velocity and pressure field satisfying

$$(\widehat{\boldsymbol{u}} \cdot \boldsymbol{\nabla})\widehat{\boldsymbol{u}} = -(0, \partial_y, \partial_z)^{\mathrm{T}}\widehat{p} + (\partial_{yy}^2 + \partial_{zz}^2)\widehat{\boldsymbol{u}}, \quad \boldsymbol{\nabla} \cdot \widehat{\boldsymbol{u}} = 0. \tag{4.2a,b}$$

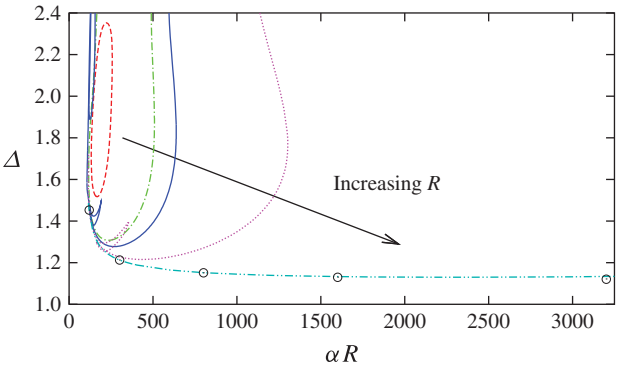

FIGURE 6. (Colour online) Variation of the wall drag Δ with the scaled wavenumber αR. The definition of the curves is the same as in figure 1.

The wave is now no longer decoupled from the roll–streak flow, and therefore the streamwise dependence is no longer confined to the fundamental streamwise mode. In order to check this assertion at small α, it is instructive to look at the energy of the wave part of the solution in figure 1(*c*). We recall that VWI states are typified by the wave energy being exclusively concentrated in the fundamental mode. On the lower part of the curves we observe that when the long-wavelength regime is established, the energy cascades into higher streamwise harmonics, as DHW showed, and indeed the solutions yield a localized appearance in the streamwise direction, associated with energy spectra where the energy is distributed away from the fundamental mode.

In figure 6 we replot the results of figure 1(*a*,*b*) in terms of the long-wave parameter αR. We see that the large-R lower-branch solutions initially connect with the HS curve at $\alpha R \gg 1$ and then follow the DHW long-wavelength results, i.e. $\alpha \sim R^{-1}$ for some intervals. The curve turns sharply upward around $\alpha R \approx 110$ and then enters the snaking region. All of the limiting structures exist well above the energy stability criteria $\alpha R \approx 49.272$ obtained in DHW. When the wavenumber formally becomes $O(R^{-1})$, the critical layer thickens out and fills the whole channel. The results of figure 3(*d*) for $\alpha = 0.05$ signal the emergence of the lower-branch long-wavelength asymptotic structure where the critical-layer singularity in VWI is lost.

A similar energy transfer also occurs on the upper part of the curve in figure 2 but at slightly higher values of α than for the lower part. In contrast to the DHW long-wavelength states, this upper-branch long-wavelength structure appears not to approach $\alpha \sim R^{-1}$ at small α and now has a wave field vertically concentrated in the y–z plane, as seen in figure 3(*a*). The boundaries between cells now appear to be straddled by jets from one side of the channel to the other. This jet-like behaviour then causes the streak to be essentially stagnant away from the jets and in thin boundary layers where the up/downwelling jets connect at $y = \pm 1$. Thus the roll–streak flow appears to have boundary layers along the top and bottom walls connected by jets between cells. Figure 7(*a*) shows that the rolls away from the jets and the boundary layers have constant vorticity, suggesting the presence of an inviscid vortex core for the roll component. The waves are excited at the roll cell boundary, as shown in figure 7(*b*), probably to account for the roll vorticity jump induced by the Reynolds stresses. The λ_2 criterion shown in figure 7(*c*) indicates that there are strong vortex structures associated with the vertical jets, where once again the roll drives the streak flow. We speculate that there is an asymptotic structure driven by

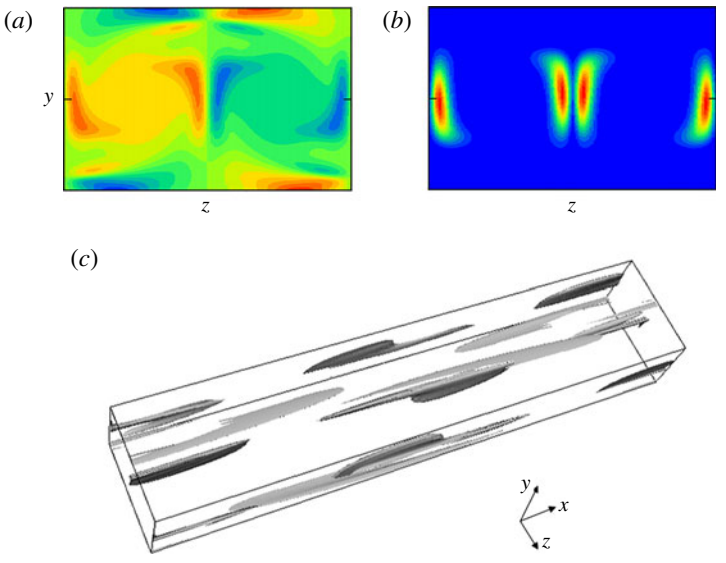

FIGURE 7. (Colour online) Flow visualization of the upper-branch solution for $(R, \alpha, \beta) = (16\,000, 0.4, 2)$. (*a*) The roll vorticity $(\partial_z V - \partial_y W)$. (*b*) The streamwise averaged energy associated with the wave component. (*c*) The 30 % minimum isosurface of λ_2; see Jeong & Hussain (1995) for the definition of this value. The truncation levels in the x, y and z directions used for the solution were 15, 70 and 30, respectively.

a wave instability of the combined roll–streak flow in the thin vertical regions where the jets are concentrated. The numerical results suggest $\alpha \sim R^{-a}$ with some $0 < a < 1$ for the new asymptotic structure. However, numerical estimation of the power a is difficult since the asymptotic convergence to the new structure is apparently not yet achieved in our calculations.

Finally, we concentrate on the excursions of the solutions from the DHW asymptotic long-wavelength states in order to shed light on the nature of the snaking behaviour of our solutions. The solid line shown in figure 8(*a*) is a close-up of the snaking branch for $R = 500$ presented in figure 1(*a*). It is found that at some point on the branch the energy E_n is concentrated at some $n \neq 1$. The filled circles labelled 'b' and 'c' are examples of such points for $n = 3$ and 5, respectively. Panels (*b*) and (*c*) of figure 8 show the flow structure for these points (left plots) and nearby VWI states duplicated three and five times in the streamwise direction (right plots); the corresponding solution branches are indicated in figure 8(*a*) by dashed and dotted lines. The contours of streamwise velocity at the midplane $y = 0$ reveal that the flow regime takes on slightly modulated subharmonic VWI-like structures at these points. In other words, the long-wavelength states are contaminated by VWI states beyond the DHW state and the long-wavelength upper-branch as-yet-unknown asymptotic state. At the points on the bifurcation curve where E_n is not concentrated in the $n = 1$ component, the flow field is 'synchronized' to subharmonic pure VWI states. Note that only odd numbers of n are allowed due to the shift–refection symmetry $[u, v, w](x, y, z) = [u, v, -w](x + \pi/\alpha, y, -z)$ of the solution preserved along the overall solution branch.

The entanglement between the VWI and pure long-wavelength DHW asymptotic states will be enhanced as R increases, since the corresponding solution branches

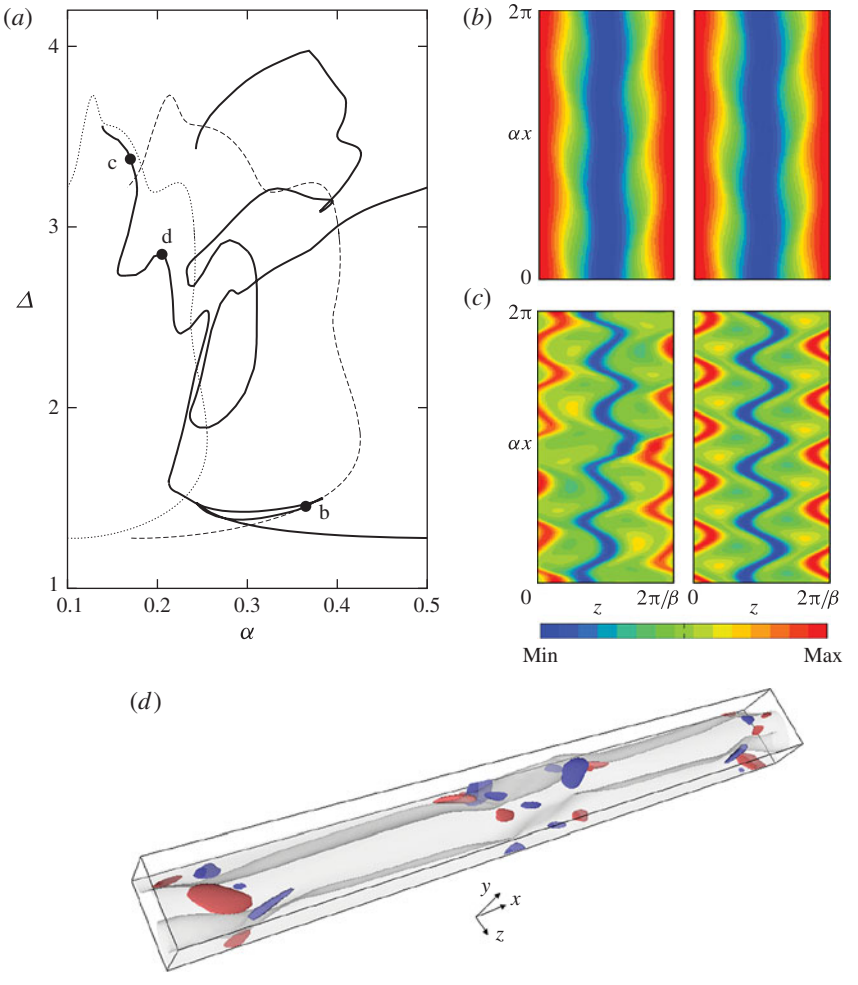

FIGURE 8. (Colour online) (*a*) Close-up of the snaking solution branch for $R = 500$ (solid curve), plotted together with the same solution branches for the three- and five-times duplicated streamwise subharmonic cases (dashed and dotted curves), to show synchronization of long-wavelength states to VWI states; the filled circles labelled 'b', 'c' and 'd' correspond to the visualizations in panels (*b*), (*c*) and (*d*). (*b*,*c*) Streamwise velocity at the midplane $y = 0$, where the left plot in each panel shows the flow regime at the solid branch for $\alpha = 0.35$ and $\alpha = 0.17$, respectively, and the right plot shows the corresponding three- and five-times subharmonic solutions in the same computation domain. (*d*) Visualization of solution outside of the synchronization at $\alpha = 0.205$; the red and blue surfaces are isosurfaces of positive and negative 70 % maximum vorticity, and the transparent grey surface represents the zero-streamwise-velocity surface.

then intersect each other more often. Equating the turning point of the limiting n-times subharmonic VWI branch at $\alpha = \alpha_c n \approx 1.37n$ and the blow-up point in figure 6, we estimate that $R \approx 80n$ for the onset of the nth entanglement between them. This prediction is consistent with what we have observed up to the $n = 5$ modulated state for $R = 500$. Notice that this tentative explanation of the origin of the entangled region associated with lower-branch VWI states does not directly apply to the upper-branch small-wavenumber states, since as yet we do not know the

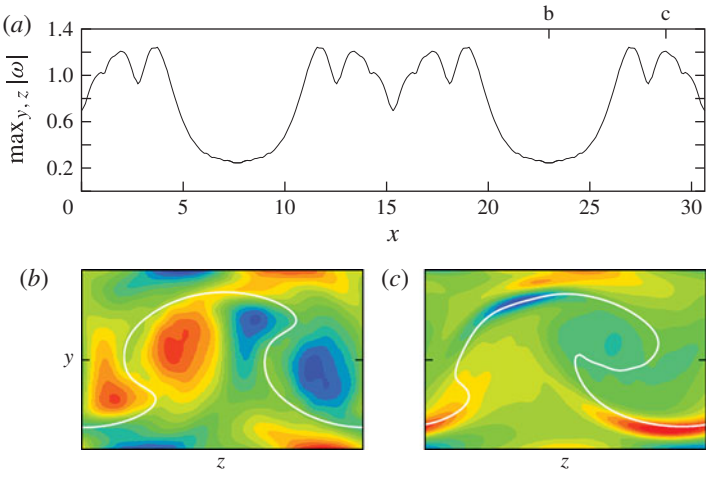

FIGURE 9. (Colour online) Streamwise vorticity of the solution labelled 'd' in figure 8(*a*); here $(R, \alpha) = (500, 0.205)$. (*a*) Variation of the in-plane maximum of the streamwise vorticity $\omega = \partial_z v - \partial_y w$ in the y–z cross-section. (*b*,*c*) Contours of the streamwise vorticity in the y–z plane at the fixed streamwise positions 'b' and 'c' in (*a*); the streamwise velocity u is zero at the white curves.

corresponding asymptotic form. Here we just note that our calculations suggest that the upper-branch long-wavelength states are also contaminated by VWI states.

For the snaking branch outside of these 'synchronized' regions, the states are related to the long-wavelength structures locally intertwined with VWI states. Figure 8(*d*) shows an example of the visualization at the point 'd' in figure 8(*a*). The streaky field indicated by the grey isosurface of zero streamwise velocity has local fluctuations where strong vorticity dominated by the wave component in VWI states arises around this surface. The streamwise vorticity can indicate whether the state is a VWI one or a long-wavelength state, since this component is dominated by the strong critical-layer structure in the former case. Strong streamwise vorticity appears when the states locally take the VWI form, as shown in figure 9(*a*). The contours of the streamwise vorticity in the y–z plane, pictured in figure 9(*b*,*c*), indeed show the existence and non-existence of the critical-layer structure at the VWI and non-VWI positions. If we consider the localized VWI-like states, each of which emerges on a streamwise scale of $O(1)$, to be embedded in the smoother structure governed by (4.2), the localized fluctuations can potentially be separated by up to $O(R)$ distances in the streamwise direction, and the DHW long-wavelength states connect to the VWI states. A phase-equation approach can be used to embed the wave part of the VWI states in slowly varying vortex fields. The wave has a local wavenumber $\alpha(X)$, and the limit state $\alpha \to 0$ in figure 1(*c*) would match the solution to the long-wavelength regime.

5. Conclusion

In view of the above numerical results, we conclude that at an $O(1)$ streamwise wavenumber the lower- and upper-branch solutions discussed in the self-sustained process literature all deform into VWI states as R increases. Therefore, the upper-branch modes have no distinct asymptotic structure as was speculated in HS; that this part of the VWI curve was not captured by HS may be due to the inadequacy of the

iteration scheme used in that paper, as opposed to Newton iteration used here. The VWI equations are fully nonlinear and thus we can expect many other VWI solutions corresponding to the Navier–Stokes solution families listed in Gibson *et al.* (2009).

The VWI asymptotic structure breaks down at asymptotically small values of the streamwise wavenumber α. The limit for the lower branch corresponds to the long-wavelength states in DHW emerging when $\alpha \sim R^{-1}$. In addition, the numerical results indicate a new long-wavelength structure characterized by vertical jets for the upper branch. The upper-branch VWI state approaches the new asymptotic states more slowly than does the lower-branch one as R increases, suggesting that the new states have wavelength scale between the VWI and DHW states.

Further, we note that a new rich variety of long-wavelength states associated with snaking behaviour of the solution branch has been found. The snaking happens when the asymptotic long-wavelength states try to locally mimic the $O(1)$-wavelength VWI solutions, thereby providing a theoretical framework of different streamwise scale coexistence phenomena in shear flows. The entanglement is enhanced as R increases, so for large R the corresponding flow structure may never take on exactly the long-wavelength asymptotic states. This theoretical explanation of streamwise scale separation can be applied to any parallel shear flow; thus, a connection to the turbulent puff phenomenon repeatedly demonstrated in pipe flow is of interest (Avila *et al.* 2013).

We believe that the results discussed in this paper are typical of any given $O(1)$ spanwise wavenumber, and for small spanwise wavenumber, spanwise localization occurs as found by, for example, Duguet, Schlatter & Henningson (2009), Schneider *et al.* (2010) and DHW. Extension of the present results in this direction would provide a rich class of localized states, perhaps having relevance to the formation of turbulent spots frequently observed in shear flows. The mechanism behind the snaking behaviour of our solution branch would be similar to the homoclinic snaking found by Schneider *et al.* (2010), where the snaking is caused by spanwise localization of disturbance, although the snaking branch is not ordered in our case since the VWI and long-wavelength states compete. Both snaking phenomena are due to the spatial scale separation of the flow field locally intertwined with VWI states of $O(1)$ length scale.

Acknowledgements

This work was supported by EPSRC under programme grant EP/I037946/1.

REFERENCES

AVILA, M., MELLIBOVSKY, F., ROLAND, N. & HOF, B. 2013 Streamwise-localized solutions at the onset of turbulence in pipe flow. *Phys. Rev. Lett.* **110**, 224502.

BLACKBURN, H. M., HALL, P. & SHERWIN, S. J. 2013 Lower branch equilibria in Couette flow: the emergence of canonical states for arbitrary shear flows. *J. Fluid Mech.* **721**, 58–85.

DEGUCHI, K., HALL, P. & WALTON, A. G. 2013 The emergence of localized vortex–wave interaction states in plane Couette flow. *J. Fluid Mech.* **721**, 58–85.

DUGUET, Y., SCHLATTER, P. & HENNINGSON, D. S. 2009 Localized edge states in plane Couette flow. *Phys. Fluids* **21**, 111701.

GIBSON, J. F., HALCROW, J. & CVITANOVIC, P. 2009 Equilibrium and travelling-wave solutions of plane Couette flow. *J. Fluid Mech.* **638**, 243–266.

HALL, P. & SHERWIN, S. 2010 Streamwise vortices in shear flows: harbingers of transition and the skeleton of coherent structures. *J. Fluid Mech.* **661**, 178–205.

HALL, P. & SMITH, F. T. 1989 Nonlinear Tollmien–Schlichting/vortex interaction in boundary layers. *Eur. J. Mech. (B/Fluids)* **8** (3), 179–205.

HALL, P. & SMITH, F. T. 1990 Near-planar TS waves and longitudinal vortices in channel flow: nonlinear interaction and focussing. In *Instability and Transition*, pp. 5–39. Springer.

HALL, P. & SMITH, F. T. 1991 On strongly nonlinear vortex/wave interactions in boundary-layer transition. *J. Fluid Mech.* **227**, 641–666.

ISONI, A. 2014 Vortex wave interaction theory to understand self-sustaining processes in transitional flows. PhD thesis, Department of Aeronautics, Imperial College London, UK.

ITANO, T. & TOH, S. 2001 The dynamics of bursting process in wall turbulence. *J. Phys. Soc. Japan* **70**, 703–716.

JEONG, J. & HUSSAIN, F. 1995 On the identification of a vortex. *J. Fluid Mech.* **285**, 69–94.

KREILOS, T. & ECKHARDT, B. 2012 Periodic orbits near onset of chaos in plane Couette flow. *Chaos* **22**, 047505.

NAGATA, M. 1990 Three-dimensional finite-amplitude solutions in plane Couette flow: bifurcation from infinity. *J. Fluid Mech.* **217**, 519–527.

SCHNEIDER, T. M., GIBSON, J. F. & BURKE, J. 2010 Snakes and ladders: localized solutions of plane Couette flow. *Phys. Rev. Lett.* **104**, 104501.

SKUFCA, J. D., YORKE, J. A. & ECKHARDT, B. 2006 Edge of chaos in a parallel shear flow. *Phys. Rev. Lett.* **96**, 174101.

WALEFFE, F. 1997 On a self-sustaining process in shear flows. *Phys. Fluids* **9**, 883–900.

WALEFFE, F. 2003 Homotopy of exact coherent structures in plane shear flows. *Phys. Fluids* **15**, 1517–1534.

WANG, J., GIBSON, J. & WALEFFE, F. 2007 Lower branch coherent states in shear flows: transition and control. *Phys. Rev. Lett.* **98**, 204501.